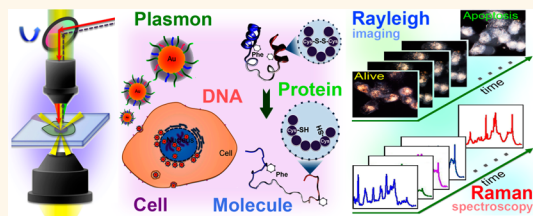


Observing Real-Time Molecular Event Dynamics of Apoptosis in Living Cancer Cells using Nuclear-Targeted Plasmonically Enhanced Raman Nanoprobes

Bin Kang,^{†,‡} Lauren A. Austin,[‡] and Mostafa A. El-Sayed^{*}

Laser Dynamics Laboratory, School of Chemistry and Biochemistry, Georgia Institute of Technology, Atlanta, Georgia 30332-0400, United States. [†]These authors contributed equally. [‡]Present address: College of Material Science and Technology, Nanjing University of Aeronautics and Astronautics, Nanjing 210016, P.R. China.

ABSTRACT Apoptosis is a biological process that plays important roles in embryogenesis, aging, and various diseases. During the process of apoptosis, cells undergo a series of morphological and molecular events such as blebbing, cell shrinkage, proteolysis, and nuclear DNA fragmentation. Investigating these events on a molecular level is crucial for gaining a more complete understanding of the intricate mechanism of apoptosis; however, the simultaneous direct observation of morphological and molecular events in real-time on a single living cell scale still remains a challenge. Herein, we directly monitored morphological and molecular events during cellular apoptosis in real-time after the treatment of an apoptosis-inducing agent, by utilizing our previously described plasmonically enhanced Rayleigh/Raman spectroscopic technique. Spectroscopic analysis of the DNA/protein composition around the cell nucleus revealed the occurrence and dynamics of three apoptotic molecular events: protein denaturation, proteolysis, and DNA fragmentation. The molecular event dynamics were used to create a temporal profile of apoptotic events in single cells. It is found that the sequence of events occurring in the apoptotic process induced by hydrogen peroxide addition is protein denaturation through disulfide bond breakage as well as DNA fragmentation, followed in time by protein unraveling with hydrophobic amino acid exposure, and finally protein degradation. These results demonstrate the potential of using this time-dependent plasmonically enhanced vibrational imaging technique to study the detailed mechanism of other apoptosis molecular pathways induced by different agents (e.g., anticancer drugs). A note is given in the conclusion discussing the expected large difference between the SERS spectrum of biological molecules in solution and that observed in live cells which are enhanced by the plasmonic field of the aggregated nanoparticles.



KEYWORDS: Raman · Rayleigh imaging · plasmonic nanoparticles · apoptosis

Understanding bioprocesses and cellular functions on a molecular level is crucial for advancements in the fields of molecular cell biology, oncology, and pathology. In particular, cell apoptosis, or programmed cell death, is one of the most studied cellular processes as it plays an important role in normal tissue development and the advancement of many acquired diseases.^{1–3} The process of apoptosis is highly regulated by a vast number of proteins and molecular signals that initiate a series of downstream cellular and molecular events. Although the intricate molecular details involved in this pathway are not completely understood, the later stages of apoptosis can be identified by several standard events.

Blebbing, cell shrinkage, nuclear fragmentation, and the formation of apoptotic bodies have all been classified as characteristic events on the cellular level, while nuclear protein denaturation, proteolysis, and DNA fragmentation have been identified as typical events that occur during apoptosis on the molecular level.^{4–6} Real-time identification and visualization of these events could provide better insight into the overall detailed molecular mechanisms and pathways involved in cellular apoptosis.

Traditionally, the molecular changes during apoptosis are obtained through techniques such as gel electrophoresis and flow cytometry.^{7–10} While these techniques offer useful information, they are based on

* Address correspondence to melsayed@gatech.edu.

Received for review February 11, 2014 and accepted April 7, 2014.

Published online April 07, 2014
10.1021/nn500840x

© 2014 American Chemical Society

end-point analyses and do not allow for direct real-time observations. Microscopy has been extensively used to monitor qualitative morphological changes.^{11,12} Single-molecule microscopy has also provided powerful tools to study various bioprocesses and allows for real-time cellular imaging.^{13–16} While this technique has many advantages, it is limited by its use of fluorescent probes as they are highly susceptible to photobleaching in a short time and therefore reduces the time scale at which cellular processes can be monitored.¹⁷ Furthermore, the emission bands of the fluorescent probes tend to overlap, restricting the resolution of the number of processes that can be monitored simultaneously.^{18–20} Recently, time-resolved cellular imaging techniques based on vibrational spectroscopy have become influential tools in cellular biology,^{21–23} as they offer the possibility to visualize the molecular composition of a large number of subcellular compartments in real-time at the single-cell level.^{24,25} Our group has recently combined plasmonically enhanced Raman scattering spectroscopy with the ability to localize plasmonic nanoparticles at a specific organelle (e.g., the nucleus) to obtain real-time cellular imaging and molecular spectroscopy signals from anywhere within the cell for up to 24 h.^{26,27}

In the present work, we report the direct observation of morphological and molecular events during the process of externally induced cellular apoptosis by using a Rayleigh/Raman spectroscopy imaging approach, termed targeted plasmonically enhanced single-cell imaging spectroscopy (T-PESCIS). Apoptosis was induced by the addition of hydrogen peroxide (H_2O_2) to human oral squamous cell carcinoma (HSC-3) cells, and the cell nucleus was monitored with the aid of nuclear-targeted gold nanospheres. Plasmonically enhanced Rayleigh scattering images and Raman scattering spectra were taken at different time points during the apoptosis treatment. The assignments of the different observed vibrations during the apoptotic events were made from *in situ* reference profiles as well as previously known assignments. Analysis of the plasmonically enhanced Raman scattering (PERS) spectra identified vibration bands associated with DNA and protein molecules at the cell nucleus. These band changes not only indicated the occurrence of molecular events such as protein denaturation, proteolysis, and DNA fragmentation but also provided the time sequence of the occurrence of these processes, that is, the dynamic profile of H_2O_2 -induced apoptosis.

RESULTS AND DISCUSSION

Synthesis of Nuclear-Targeted Raman Nanoprobes. In order to amplify the Raman signals of molecules located at the nucleus, gold nanospheres modified with nuclear-targeting peptides were prepared. The nuclear-targeted gold nanospheres (NT-AuNSs) were synthesized by the citrate reduction method²⁸ and had an average diameter of 21 ± 6 nm (Supporting Information Figure S1).

The purified citrate-AuNSs were then conjugated with modified poly(ethylene glycol) (PEG) ligands in order to improve their stability in biological environments and inhibit nonspecific protein binding to their surface.²⁹ To increase the uptake of the AuNSs and promote their localization at the cells' nuclei, the PEG-stabilized AuNSs were further conjugated to arginine–glycine–aspartic acid (RGD) and nuclear localization signal (NLS) peptides. RGD peptides are known to target $\alpha v \beta 6$ integrins on the surface of the cell membrane and assist in receptor-mediated endocytosis.^{30,31} Thusly, the cell line used in this study, human oral squamous cell carcinoma (HSC-3) cells, overexpresses $\alpha v \beta 6$ integrins.^{32–34} NLS peptides are known to contain a characteristic lysine–lysine–lysine–arginine–lysine (KKKKR) sequence, which replicates the nuclear tag exhibited by endogenous biomolecules that are marked for nuclear translocation.^{35,36} Successful conjugation to PEG, RGD, and NLS ligands was confirmed through the changes in hydrodynamic diameter and ζ -potential measurements obtained *via* dynamic light scattering (Table S1). PEGylation led to ~ 20 nm increase in the hydrodynamic diameter and a change in ζ -potential from -20 to -18 mV when compared with citrate-AuNSs. The addition of RGD and NLS peptides to the AuNSs' surface did not alter the hydrodynamic diameter, but the ζ -potential further increased to -17 mV. Dark-field images of HSC-3 cells treated with 0.05 nM NT-AuNSs for 24 h also showed intracellular localization at the nucleus, further confirming successful synthesis of NT-AuNSs (Figure 1). It should be noted that protein corona formation on NT-AuNSs was negligible, and the UV–vis spectrum, the hydrodynamic diameter, and the ζ -potential were not significantly altered after their incubation in cell culture medium under the same conditions as those used in PERS live-cell experiments (Figure S2).

PERS Reference Profile of Induced Apoptotic Molecular Events. Apoptosis can be characterized by molecular events such as nuclear protein denaturation, proteolysis, and DNA fragmentation.^{4–6,37} Since these events involve molecular changes that have distinct Raman signatures (i.e., proteins/peptides, nucleotides, etc.), it was hypothesized that we could observe these events in real-time. Therefore, we performed a set of *in situ* experiments to create reference profiles of these events that would be used to evaluate the spectra obtained in the live-cell PERS experiments. The *in situ* PERS spectra obtained through treatment of HSC-3 protein lysates with β -mercaptoethanol and trypsin were used to detect protein denaturation and protein degradation. After treatment, protein lysates were mixed with NT-AuNSs and dried on a glass slide to acquire the Raman spectra. Figure 2 shows the resulting PERS spectra. This spectrum is significantly different from that of the NT-AuNSs alone (Figure S3), indicating the successful use of AuNSs to enhance biomolecular signals located within their plasmonic field.

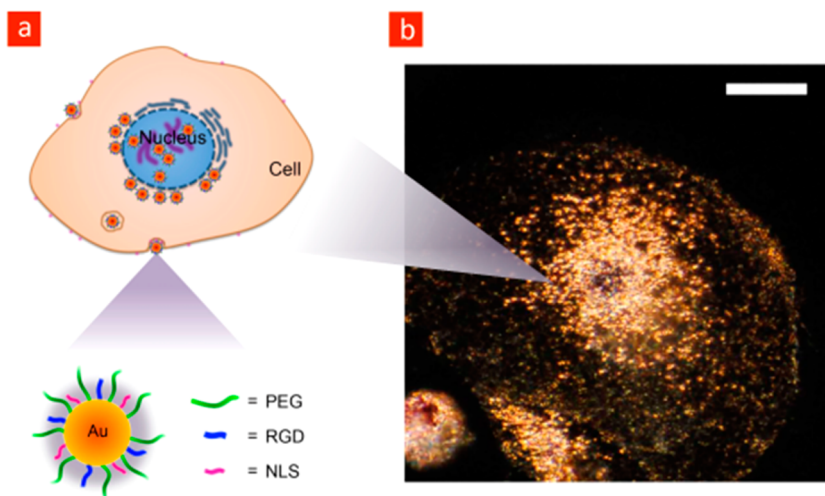


Figure 1. Design of the nuclear-targeted PERS nanoprobes. (a) Schematic diagram of the internalization and localization of the nuclear-targeted AuNSs (NT-AuNSs) that are used to enhance the Raman signals of molecules from the targeted nucleus. (b) Representative dark-field image of HSC-3 cells pretreated with 0.05 nM NT-AuNSs for 24 h. The NT-AuNSs are localized at the nucleus. Scale bar = 10 μ m.

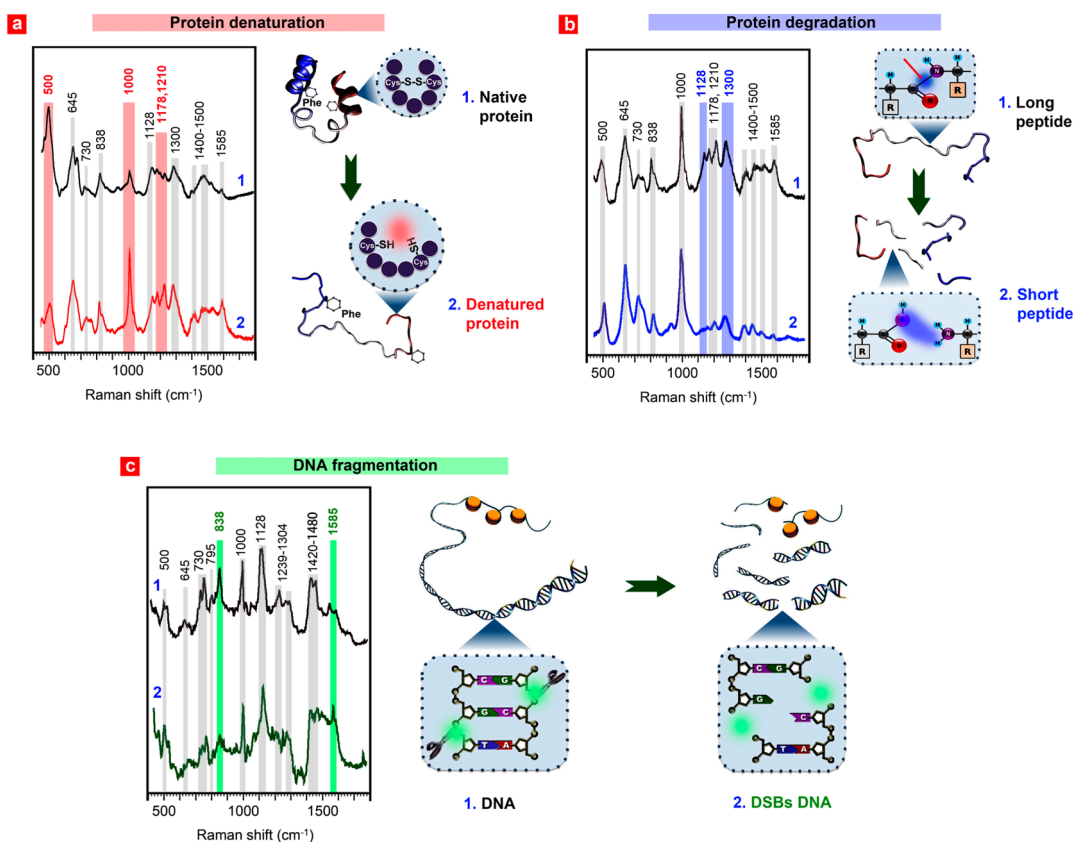


Figure 2. *In situ* reference spectra of apoptotic molecular events. (a) Protein denaturation: plasmonically enhanced Raman spectrum of highly ordered, folded proteins extracted from HSC-3 cells (top) and denatured proteins treated by β -mercaptoethanol (bottom). (b) Protein degradation: plasmonically enhanced Raman spectra of long, intact peptides (top) and short peptides treated by trypsin (bottom). (c) DNA fragmentation: plasmonically enhanced Raman spectra of undamaged, extracted DNA from cells (top) and damaged DNA in the form of double-strand breaks (DSBs) after 4 h treatment with UV light (bottom).

Lysates that were treated with only β -mercaptoethanol showed a decrease in the 500 cm^{-1} vibration and an increase in the 1000 , 1178 , and 1210 cm^{-1} vibrations (Figure 2a). Since β -mercaptoethanol is

known to disrupt the disulfide bonds,³⁸ we assigned the decrease in the 500 cm^{-1} vibration to disulfide bond ($-\text{S}-\text{S}-$) breakage and the dissolution of tertiary protein structure. With the disruption of tertiary

TABLE 1. *In Situ* Reference PERS Spectra for Apoptotic Protein Degradation, Protein Denaturation, and DNA Fragmentation

Band (cm ⁻¹)	Assignment	Band Dynamics	Indicated Molecular Changes	Identified Molecular Events
500	Disulfide bond -S-S-, Protein	↓	Disulfide bond cleavage	Protein denaturation
838	O-P-O strength, DNA backbone	↓	DNA backbone structure breakage	DNA fragmentation
1000	Ring breath, Phenylalanine	↑	Exposure of phenylalanine ring structure	Protein denaturation
1128	C-N, stretch, Peptide bond	↓	Peptide bond cleavage	Protein degradation
1178	C-H bend, C-C stretch, Tyrosine	↑		Protein denaturation
1210	C-C ₆ -H ₅ , Phenylalanine, Tryptophan	↑	Exposure of peptide/amino acid side groups	Protein denaturation
1300	Amide III	↓	Peptide amide structure breakage	Protein degradation
1585	-N ₇ -H, Guanine, Adenine	↑	Exposure of DNA bases	DNA fragmentation

structure, hydrophobic amino acids, normally positioned within the interior pockets of the protein, are no longer protected by the folded structure.^{39,40} These amino acids include phenylalanine, tyrosine, and tryptophan, which all have strong Raman vibrations due to their heavily conjugated rings. Therefore, increases in the 1000, 1178, and 1210 cm⁻¹ vibrations previously assigned to phenylalanine's benzene ring breathing,^{23,41} tyrosine's C—H bending and C—C stretching,⁴² and phenylalanine and tryptophan's C—C₆—H₅ stretching,⁴³ respectively, are attributed to the exposure of these amino acids to the AuNSs' plasmonic field after protein unfolding. These reference bands, 500, 1000, 1178, and 1210 cm⁻¹, are observed during the apoptosis process studied in the present work and signal a protein denaturation process in our HSC-3 live-cell PERS experiments (Table 1). In addition to the above characterized protein bands, bands around 645, 1128, 1300, and 1400–1500 cm⁻¹ are also observed, which could be assigned to the C—S, C—N, amide III, and amide II bands of proteins.^{39–41}

Protein lysates that were treated with β -mercaptoethanol followed by trypsin exhibited a significant decrease in the 1128 and 1300 cm⁻¹ vibrations, in addition to those changes seen with β -mercaptoethanol treatment alone (Figure 2b). These vibrations were assigned to the C—N stretching and the amide III stretching of peptide bonds,^{42,43} respectively. As trypsin is a known serine protease,⁴⁴ cleaving peptides on the carboxyl side of lysine and arginine amino acids, we assigned the decreases in 1128 and 1300 cm⁻¹ vibrations to peptide bond hydrolysis (i.e., protein degradation). These reference band changes, a decrease

in 1128 and 1300 cm⁻¹, will be used to evaluate proteolysis in our live-cell PERS experiments (Table 1).

Similar to the protein denaturation and degradation profiles, we conducted *in situ* experiments to obtain reference PERS spectra of DNA fragmentation. DNA fragmentation in the form of DNA double-strand breaks (DSBs) was induced via UV irradiation (\sim 4 h) in genomic DNA extracted from HSC-3 cells.⁴⁵ After UV treatment, DNA extracts were directly mixed with NT-AuNSs and dried on a glass slide to obtain PERS spectra. The spectra revealed pronounced bands at 730, 795, 838, 1239–1304, 1420–1480, and 1585 cm⁻¹, which were assigned to the nucleic acid adenine,²³ cytosine, and thymine,²³ O—P—O backbone,²⁵ deoxynucleotides,²⁵ C—H deformation of guanine and adenine,⁴⁶ and N₇—H stretch of guanine and adenine,⁴⁷ respectively (Figure 2c). Bands were also observed at 500, 645, 1000, and 1128 cm⁻¹, but these are associated with proteins that remain in the DNA extracts after isolation. After UV exposure, the 838 cm⁻¹ O—P—O backbone vibrations decreased, while the 1585 cm⁻¹ N₇—H vibration of guanine and adenine significantly increased. The increase in guanine and adenine vibrations after the formation of DNA DSBs is associated with their increased exposure to the plasmonic field of NT-AuNSs during detachment of DNA from the histone proteins. These alterations suggest the formation of DNA DSBs, and the reference bands at 838 and 1585 cm⁻¹ will be used to follow the DNA fragmentation process during apoptosis in the live-cell experiments (Table 1).

Following Apoptotic Temporal Events in Dying Cells Using the T-PESCI Technique. To allow for the acquisition of live-cell PERS spectra at the nucleus, a homemade live-cell

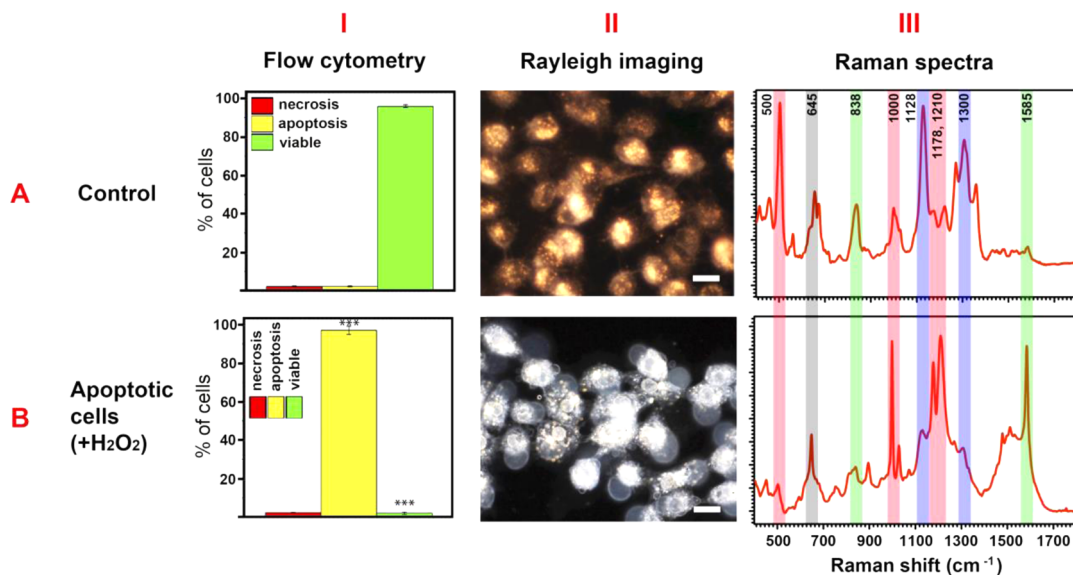


Figure 3. Viable and apoptotic cells produce different T-PESCIS images and spectra. Flow cytometric analysis (I), plasmonically enhanced Rayleigh scattering images (II), and plasmonically enhanced Raman spectra (III) of untreated viable cells (A) and apoptotic cells treated with $100 \mu\text{M}$ H_2O_2 (B).

imaging chamber was used in conjunction with a Raman spectrometer equipped with dark-field Rayleigh scattering imaging optics (Figure S4). This setup coupled with the prepared NT-AuNSs enables Rayleigh live-cell scattering images and Raman molecular spectra from biomolecules near the nucleus to be obtained simultaneously in real-time. By comparing the cellular morphology and the molecular spectroscopic changes before and after the addition of an apoptosis-causing agent, it is possible to determine the molecular events associated with the process of cellular apoptosis.

The induction of apoptosis in HSC-3 cells was achieved by a $100 \mu\text{M}$ H_2O_2 treatment, as it is known to cause apoptosis *via* oxidative stress.^{48,49} Apoptosis in HSC-3 cells, after drug treatment for 24 h, was confirmed by flow cytometric analysis (Figure 3I), and particle internalization was indicated by the observation of the strong scattered light seen at the nucleus in the Rayleigh images of the cells (Figure 3II). The internalized NT-AuNSs aggregated once inside the cells, which caused a shift in the SPR scattering peak from 524 nm to the strong peak at 600–700 nm.²⁶ For apoptotic treatments, the cell morphology was significantly altered (*i.e.*, cell shrinkage, blebbing, etc.), and the shrunken cells exhibited strong white Rayleigh scattering light. These morphological changes suggest the appearance of an apoptotic cell, and the strong white Rayleigh scattering suggests that the dead cell has lifted off the substrate and intracellular components have aggregated.⁵⁰ In order to enhance intracellular Raman signals, without inhibiting cell functions and viability, HSC-3 cells were exposed to 0.05 nM NT-AuNSs for 24 h before cell death induction.²⁷

When we compared the Raman spectra of apoptotic and viable cells after 24 h of H_2O_2 treatment (Figure 3), there were several notable spectroscopic changes that correlated with our reference profiles from *in situ* PERS experiments. The intensity of the sharp band at 500 cm^{-1} decreased, while the intensity of the 1000 , 1178 , and 1210 cm^{-1} bands increased. Since these changes were seen after protein denaturation using β -mercaptoethanol, the decrease in the 500 cm^{-1} vibration indicates disulfide bond breakage within intracellular proteins and loss of their tertiary structure. The parallel increase in 1000 , 1178 , and 1210 cm^{-1} bands further indicates the loss of protein tertiary structure and protein denaturation as these bands indicate that hydrophobic amino acids, phenylalanine, tryptophan, and tyrosine, are no longer positioned and protected within the interior of a highly folded protein. Pronounced decreases in the relative intensities of the 1128 and 1300 cm^{-1} vibrations were also seen after apoptotic treatment. As these vibration changes were previously determined to indicate peptide bond hydrolysis through *in situ* serine protease treatment, these bands indicate that apoptotic treatment resulted in degradation of proteins located at the nucleus. Lastly, the 838 cm^{-1} band intensity decreased, while that of the 1585 cm^{-1} band increased. Since these vibrations were attributed to DNA backbone breakage and the exposure of purine bases after *in situ* UV exposure, these band changes indicated that nuclear DNA fragmentation as a result of apoptosis was detectable using our setup.

Apoptosis Dynamics Revealed by T-PESCIS. To investigate the correlation between the real-time dynamics of the identified apoptotic molecular events, HSC-3 cells treated with $100 \mu\text{M}$ H_2O_2 were monitored for 24 h

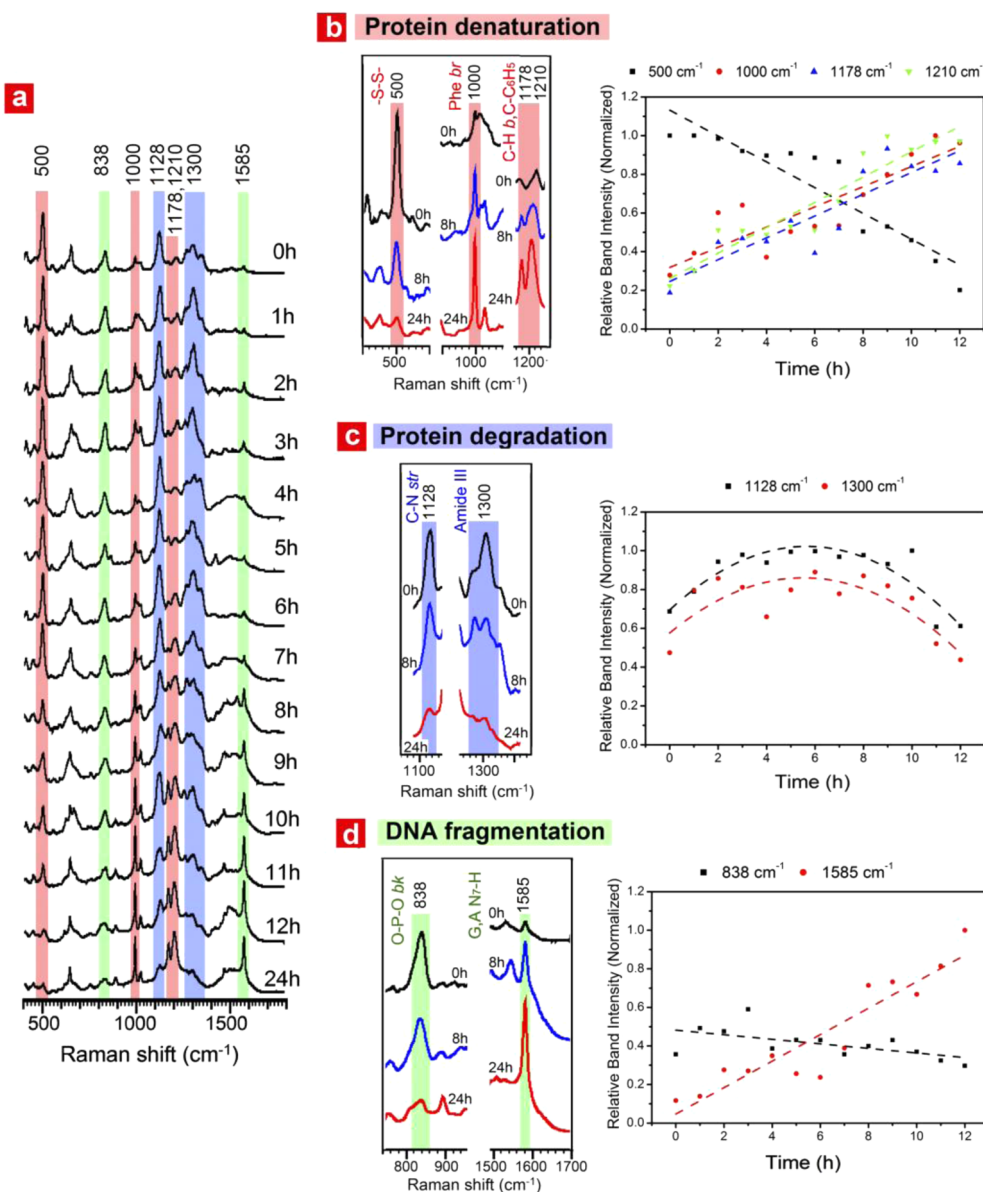


Figure 4. Dynamic profile of molecular events during oxidative stress induced apoptosis. (a) Real-time plasmonically enhanced Raman spectra of cell apoptosis induced by $100 \mu\text{M H}_2\text{O}_2$. (b-d) Raman band intensities versus time associated with different molecular events during cellular apoptosis caused by H_2O_2 .

using T-PESCS (Figure 4a). The relative intensities of the eight Raman vibrations ($500, 838, 1000, 1128, 1178, 1210, 1300, 1585 \text{ cm}^{-1}$) identified through *in situ* and end-point PERS analysis were plotted *versus* time. As seen in Figure 4b, protein denaturation occurs following zero-order kinetics. When we compared the event rates of protein denaturation, disulfide bond breakage, and exposure of hydrophobic amino acids, it was clear that disulfide bonds stabilizing a protein's tertiary structure were severed before the exposure of interior amino acids (Table 2). This agrees well with reports in literature and demonstrates the sensitivity of T-PESCS for real-time analysis of biomolecular events. Disulfide bond breakage occurs at a rate of -0.066 h^{-1} ($1.17 \times 10^{-3} \text{ min}^{-1}$) and indicates that the half-life of nuclear protein tertiary structure is 7.6 h. As expected, the

vibrations relating to hydrophobic amino acid exposure occurred at similar rates ($1000 \text{ cm}^{-1}, 0.052 \text{ h}^{-1}$; $1178 \text{ cm}^{-1}, 0.056 \text{ h}^{-1}$; and $1210 \text{ cm}^{-1}, 0.066 \text{ h}^{-1}$) and have delays in their half-lives by $\sim 1\text{--}2$ h when compared to that of disulfide bond breakage. The analysis of protein degradation vibrations over time was broken down into two time intervals (0–6 and 6–12 h) to obtain rate constants and associated half-lives (Figure 4c, Figure S5, and Table 2). As the 1128 and 1300 cm^{-1} bands are assigned to peptide bond vibrations, the initial increase in their relative band intensities was associated with the loss of protein tertiary structure and the exposure of the peptide bond to the plasmonic field of the PERS nanoprobes, which enabled us to detect it by the plasmonic enhancement technique. After the initial increase, the relative

TABLE 2. Real-Time Dynamics of Late-Stage Apoptotic Events in HSC-3 Cells Treated with 100 μ M H₂O₂

Band (cm ⁻¹)	Assignment	Rate (h ⁻¹)	Half-life (h)
500	Disulfide bond -S-S-, Protein	-0.066 +/- 0.008	7.6
838	O-P-O strength, DNA backbone	-0.011 +/- 0.005	22.7
1000	Ring breath, Phenylalanine	-0.052 +/- 0.008	9.6
1128	C-N, stretch, Peptide bond	0.048 +/- 0.012 -0.066 +/- 0.022	3.1 2.3
1178	C-H bend, C-C stretch, Tyrosine	0.056 +/- 0.008	8.9
1210	C-C ₆ -H ₅ , Phenylalanine, Tryptophan	0.066 +/- 0.007	7.6
1300	Amide III	0.038 +/- 0.024 -0.071 +/- 0.018	6.6 3.5
1585	-N ₂ -H, Guanine, Adenine	0.069 +/- 0.008	7.2

intensities decreased, and this was associated with peptide bond cleavage. Together, these data reveal that the hydrolysis of peptide bonds occurs only after disulfide bond breakage and the loss of the tertiary structure. Interestingly, the vibrations describing DNA fragmentation occur at drastically different rates (838 cm⁻¹, -0.012 h⁻¹ and 1585 cm⁻¹, 0.069 h⁻¹). From zero-order rate analysis, the exposure of purine bases appears to occur \sim 3.1 times faster than the DNA backbone cleavage (Figure 4d). This apparent reverse in the sequence of DNA fragmentation events could be attributed to the DNA damage response mechanisms. When cells are subjected to UV irradiation, DNA DSBs result, followed by rapid phosphorylation of Ser139 in γ -H2AX.^{51,52} It is the phosphorylation at Ser139 that is thought to skew the apparent rate in DNA phosphate backbone breakage. It is possible that further analysis of the rates of these two events could lead to a real-time detection assay of DNA DSBs in single living cells.

CONCLUSION

We reported the direct observation of molecular events in real-time during the process of externally induced apoptosis in HSC-3 cancer cells by using Rayleigh and Raman spectral imaging using the T-PES-CIS technique. Real-time monitoring of the structural changes on the molecular level in the form of DNA/protein complexes was achieved by taking the plasmonically enhanced Rayleigh scattering images and the Raman spectra from molecules around the cell's nuclear region targeted with gold nanospheres containing NLS peptides. The vibration assignments for these events were made from previously known vibration assignments as well as from designed *in situ*

experiments. Through Raman band analysis, three molecular events (*i.e.*, protein denaturation, protein degradation, and DNA fragmentation) were distinguished, and the dynamics of these events were obtained. The temporal profile of these events allowed a sequence of events in real-time to be established: (1) protein disulfide bond breakage along with DNA fragmentation; (2) hydrophobic amino acid and peptide bond exposure (*i.e.*, loss of tertiary structure); and (3) peptide bond hydrolysis. This work offers a new possibility to monitor in real-time multi-molecular events *via* molecular vibrations of various biomolecules in living cells. By altering the targeting strategy of AuNSs to localize the plasmonic enhancement at different intracellular locations and expanding the analysis of the recorded Raman spectra, it is reasonable to expect the simultaneous tracking of multiple molecular events in real-time. It is hoped that this technique would enable future computational theoretical scientists to propose possible detailed biological mechanisms of these important processes.

Moreover, this work has shown that a large difference could be observed between the SERS spectra of biological molecules in solution and those molecules within living (or dead) cells that are enhanced by the plasmonic field of aggregated gold or silver nanoparticles. There are two distinct differences. First, there is a difference in the distribution of the biological molecules in the living cells and in the *in situ* experiments. Second, there is a large difference in the plasmonic field distribution in the *in situ* experiment and that resulting from the aggregated nanoparticles in the cell. These two effects make it difficult to expect or to observe the exact same pattern for proteins or DNA

bands appearing with the same relative intensities in the two experiments. Of all the Raman-active bands observed in the *in situ* SERS spectrum, only those

molecules in the cell that are present in the plasmonic field of the aggregated Au or Ag nanoparticles will be observed.

METHODS

AuNS Synthesis. Citrate-stabilized AuNSs with an average diameter of 21 nm were synthesized by the reduction of gold ions (HAuCl_4) with trisodium citrate.²⁸ A 475 mL solution of 1.6 mM HAuCl_4 was heated to 100 °C under continuous stirring. Immediately after the gold solution reached 100 °C, 25 mL of 18.0 mM trisodium citrate was added. Once the color change from colorless to red was observed, heating and stirring were terminated, and the solution was allowed to reach room temperature. AuNSs were washed using DI water as the dispersant *via* centrifugation at 6000 rpm for 15 min. TEM analysis indicated that the nanospheres had an average particle diameter of 21 ± 6 nm, and UV-vis spectroscopy showed a surface plasmon resonance band at 530 nm (Figure S1). TEM images were acquired with a JEOL 100CX-2 transmission electron microscope, and the average particle diameter was determined using ImageJ.

AuNS PEGylation and Peptide Conjugation. Thiol-modified poly(ethylene glycol) (PEG, MW = 5000) was utilized on the AuNSs' surface to reduce aggregation and nonspecific binding of proteins when the AuNSs were used in biological settings.²⁹ PEGylation was conducted to obtain 10^3 molar excess of PEG ligands on the AuNSs' surface using a 1.0 mM solution of mPEG-SH 5000 (Laysan Bio, Inc.) prepared in DI water. The PEG-AuNSs were allowed to incubate overnight at room temperature under gentle shaking. The PEGylated AuNSs were centrifuged one time at 6000 rpm for 15 min, and particle pellets were redispersed in DI water. Successful surface modification with PEG was assessed using UV-vis spectroscopy and dynamic light scattering (DLS) (Table S1).

After successful modification with PEG, AuNSs were conjugated with RGD and NLS peptides following a previously established method.^{50,53} Both peptides were purchased from GenScript under custom order to attain C-terminal amidation. A 5.0 mM RGD (CGPDGRDGRDGRDGR) peptide solution and a 5.0 mM NLS (GGVKKKKPGG) peptide solution were added to purified PEG-AuNSs to achieve 10^4 and 10^5 molar excess, respectively. The solution was allowed to incubate overnight under gentle shaking at room temperature. The peptide-conjugated PEG-AuNSs were cleaned *via* centrifugation (14 000 rpm, 5 min). AuNSs were redispersed in DI water, and the success of peptide conjugation was confirmed through UV-vis spectroscopy and DLS (Table S1). Spectra obtained after each conjugation showed a slight red shift indicating the change in the dielectric constant of the AuNSs' surrounding environment. DLS measurements indicated a ~ 20 nm increase in diameter after PEGylation and an increase in the ζ -potential after each conjugation. Stock NLS/RGD-AuNSs were diluted in supplemented DMEM cell culture medium to achieve the desired treatment concentration.

Protein Corona Analysis. A volume of the stock NT-AuNS was diluted in supplemented DMEM culture medium to achieve a final concentration of 0.05 nM. The diluted NT-AuNS solution was then incubated for 24 h at 37 °C in a 5% CO_2 humidified incubator to mimic conditions in live-cell PERS experiments. After incubation, the nanoparticle solution was washed three times in DI water using centrifugation at 14 000 rpm for 3 min. UV-vis spectroscopy and DLS were used to assess protein corona formation on the NT-AuNSs (Figure S2).

Cell Culture. Human oral squamous cell carcinoma (HSC-3) cells, malignant epithelial cells, were cultured in Dulbecco's modified Eagle's medium (DMEM) (Mediatech) supplemented with 4.5 g/L glucose and sodium pyruvate, 10% v/v fetal bovine serum (FBS) (Mediatech), and 1% antimycotic solution (Mediatech). Cell cultures were maintained at 37 °C in a 5% CO_2 humidified incubator.

Protein Extraction and Denaturation/Degradation. HSC-3 cells were seeded in 12-well plates for 24 h and then exposed to 0.05 nM NLS/RGD-AuNSs for an additional 24 h. After particle treatment, cells were washed two times in cold DPBS and treated with 100 μL of 1× cell lysis buffer (Cell Signaling Technology) supplemented with 1 mM PMSF. Cells were incubated for 5 min at 4 °C and then scraped to damage the cellular membrane. Lysate solutions were combined and centrifuged at 14 000 rpm for 5 min. For protein denaturation, after centrifugation, the pellets were discarded and the lysate solutions were subjected to 5% β -mercaptoethanol and 100 °C heat for 5 min. Denatured lysates were then mixed with 5 μL of 12.1 nM NLS/RGD-AuNS solution and dried on a Raman sample holder. For protein degradation, after protein denaturation was induced, lysates were incubated in a 1:1 ratio of lysate/trypsin at 37 °C for 7 min. Once trypsinization was completed, degraded lysates were mixed with 5 μL of 12.1 nM NLS/RGD-AuNS solution and dried on a Raman sample holder.

Genomic DNA Extraction and Damage. HSC-3 cells were grown in 12-well plates for 24 h and then treated with 0.05 nM NLS/RGD-AuNSs for another 24 h. After particle incubation, cells were trypsinized and collected *via* centrifugation at 1500 rpm for 7 min. Genomic DNA was extracted using the Mammalian Genomic DNA Miniprep Kit (Sigma-Aldrich). DNA damage was induced by UV irradiation for 4 h. After 4 h, genomic DNA was mixed with 5 μL of 12.1 nM NLS/RGD-AuNS solution and dried on a Raman sample holder.

Annexin V—Propidium Iodide Staining. HSC-3 cells were grown in 12-well plates for 24 h and then pretreated with 0.05 nM NLS/RGD-AuNSs for an additional 24 h. After pretreatment, the NLS/RGD-AuNS solutions were removed and the desired concentration of H_2O_2 (BDH Aristar Ultra) was added. Treatment solutions were allowed to incubate with HSC-3 cells for 48 h. Particle solutions were replaced with complete DMEM for 48 h to ensure the same growth period as untreated cells and cells treated with H_2O_2 . Cells were collected after trypsinization and washed twice with cold DPBS. After the final wash, cells were redispersed in 1× Annexin V binding buffer, and 5 μL of Annexin V–FITC and 2 μL of propidium iodide (PI) were added. Cell solutions were incubated for 15 min at room temperature and immediately run on a BSR LSR II flow cytometer (BD Biosciences). Samples were excited with a 488 nm laser, and FITC was detected in FL-1 by a 525/30 BP filter while PI was detected in FL-2 by a 575/30 BP filter. Standard compensation using single-stained and unstained cells was done prior to running experiments. Determination of apoptotic, necrotic, and live-cell populations on at least 10 000 events was conducted with FlowJo (Tree Star Inc.), a flow cytometry analyzing software.

T-PESCISS Studies. HSC-3 cells were cultured on 18 mm coverslips for 24 h in supplemented DMEM cell culture medium. Cells were then exposed to 0.05 nM NLS/RGD-AuNSs for 24 h to enhance the signals. After 24 h, the cell-containing coverslips were inserted into a homemade live-cell chamber that maintained 37 °C temperature and 5% CO_2 concentration. The chamber was then placed into the T-PESCISS setup as demonstrated in Figure S4. H_2O_2 solutions prepared in supplemented DMEM cell culture medium to a final concentration of 100 μM were injected into the live-cell chamber using an autoinjection system. Rayleigh and Raman spectra were obtained for 24 h following drug injection. The T-PESCISS Raman system utilized a 785 nm excitation laser, an inverted microscope with a 50× objective lens fitted with filters to exclude signals from the laser, as well as Rayleigh scattering. The pretreatment with NLS/RGD-AuNSs enabled the acquisition of well-resolved spectra to be under 10 s when using the extended scan mode. The spectra mapping mode required <1 s. The Raman spectra use for quantitative analysis at each time point is the averaged Raman

spectra of at least 10 randomly chosen cells. Three independent T-PESCS experiments were used to obtain the final averaged Raman data that were then normalized to the most intense band. Normalized intensities of the 8 bands were plotted *versus* time (up to 12 h) and linearly fit using Origin 8.0 (Origin Laboratories, Corp.).

Statistical Analysis. Statistical analyses of experimental values are conveyed as mean \pm SEM of three independent experiments. The data were analyzed using the *t* test calculator (GraphPad Software, GraphPad Software, Inc.), and statistical significance was determined from untreated (control) to treated (H_2O_2) samples. Asterisks indicated statistically significant data with the following format: * P < 0.05, ** P < 0.01, and *** P < 0.001.

Conflict of Interest: The authors declare no competing financial interest.

Acknowledgment. Authors would like to thank NSF-DMR 3306HB3.

Supporting Information Available: Additional figures and tables as described in the text. This material is available free of charge *via* the Internet at <http://pubs.acs.org>.

REFERENCES AND NOTES

1. Edinger, A. L.; Thompson, C. B. Death by Design: Apoptosis, Necrosis and Autophagy. *Curr. Opin. Cell Biol.* **2004**, *16*, 663–669.
2. Eum, H. A.; Cha, Y. N.; Lee, S. M. Necrosis and Apoptosis: Sequence of Liver Damage Following Reperfusion after 60 min Ischemia in Rats. *Biochem. Biophys. Res. Commun.* **2007**, *358*, 500–505.
3. Ghavami, S.; Hashemi, M.; Ande, S. R.; Yeganeh, B.; Xiao, W.; Eshraghi, M.; Bus, C. J.; Kadkhoda, K.; Wiechec, E.; Halayko, A. J.; *et al.* Apoptosis and Cancer: Mutations within Caspase Genes. *J. Med. Genet.* **2009**, *46*, 497–510.
4. Elmore, S. Apoptosis: A Review of Programmed Cell Death. *Toxicol. Pathol.* **2007**, *35*, 495–516.
5. Pinton, P.; Ferrari, D.; Di Virgilio, F.; Pozzan, T.; Rizzuto, R. Molecular Machinery and Signaling Events in Apoptosis. *Drug Dev. Res.* **2001**, *52*, 558–570.
6. Rastogi, R. P.; Richa; Sinha, R. P. Apoptosis: Molecular Mechanisms and Pathogenicity. *Excl. J.* **2009**, *8*, 155–181.
7. Guttridge, D. C.; Albanese, C.; Reuther, J. Y.; Pestell, R. G.; Baldwin, A. S. Nf- κ appa B Controls Cell Growth and Differentiation through Transcriptional Regulation of Cyclin D1. *Mol. Cell. Biol.* **1999**, *19*, 5785–5799.
8. Susin, S. A.; Lorenzo, H. K.; Zamzami, N.; Marzo, I.; Snow, B. E.; Brothers, G. M.; Mangion, J.; Jacotot, E.; Costantini, P.; Loeffler, M.; *et al.* Molecular Characterization of Mitochondrial Apoptosis-Inducing Factor. *Nature* **1999**, *397*, 441–446.
9. Bortner, C. D.; Gomez-Angelats, M.; Cidlowski, J. A. Plasma Membrane Depolarization without Repolarization Is an Early Molecular Event in Anti-Fas-Induced Apoptosis. *J. Biol. Chem.* **2001**, *276*, 4304–4314.
10. Kajstura, M.; Halicka, H. D.; Pryjma, J.; Darzynkiewicz, Z. Discontinuous Fragmentation of Nuclear DNA during Apoptosis Revealed by Discrete "Sub-G1" Peaks on DNA Content Histograms. *Cytometry, Part A* **2007**, *71A*, 125–131.
11. Cohen, G. M.; Sun, X. M.; Snowden, R. T.; Dinsdale, D.; Skilleter, D. N. Key Morphological Features of Apoptosis May Occur in the Absence of Internucleosomal DNA Fragmentation. *Biochem. J.* **1992**, *286*, 331–334.
12. Häcker, G. The Morphology of Apoptosis. *Cell Tissue Res.* **2000**, *301*, 5–17.
13. Huang, B.; Wang, W. Q.; Bates, M.; Zhuang, X. W. Three-Dimensional Super-resolution Imaging by Stochastic Optical Reconstruction Microscopy. *Science* **2008**, *319*, 810–813.
14. Shav-Tal, Y.; Darzacq, X.; Shenoy, S. M.; Fusco, D.; Janicki, S. M.; Spector, D. L.; Singer, R. H. Dynamics of Single mRNPs in Nuclei of Living Cells. *Science* **2004**, *304*, 1797–1800.
15. Levsky, J. M.; Shenoy, S. M.; Pezo, R. C.; Singer, R. H. Single-Cell Gene Expression Profiling. *Science* **2002**, *297*, 836–840.
16. Sochacki, K. A.; Larson, B. T.; Sengupta, D. C.; Daniels, M. P.; Shtengel, G.; Hess, H. F.; Taraska, J. W. Imaging the Post-fusion Release and Capture of a Vesicle Membrane Protein. *Nat. Commun.* **2012**, *3*, 1154.
17. Hoebe, R. A.; Van Oyen, C. H.; Gadella, T. W. J.; Dhonukshe, P. B.; Van Noorden, C. J. F.; Manders, E. M. M. Controlled Light-Exposure Microscopy Reduces Photobleaching and Phototoxicity in Fluorescence Live-Cell Imaging. *Nat. Biotechnol.* **2007**, *25*, 249–253.
18. Xiao, J.; Yu, J.; Xie, X. S. Probing Gene Expression in Live Cells, One Molecule at a Time. *Science* **2006**, *311*, 1600–1603.
19. Yu, J.; Xiao, J.; Ren, X. J.; Lao, K. Q.; Xie, X. S. Probing Gene Expression in Live Cells, One Protein Molecule at a Time. *Science* **2006**, *311*, 1600–1603.
20. Femino, A.; Fay, F. S.; Fogarty, K.; Singer, R. H. Visualization of Single RNA Transcripts *in Situ*. *Science* **1998**, *280*, 585–590.
21. Freudiger, C. W.; Min, W.; Saar, B. G.; Lu, S.; Holtom, G. R.; He, C. W.; Tsai, J. C.; Kang, J. X.; Xie, X. S. Label-Free Biomedical Imaging with High Sensitivity by Stimulated Raman Scattering Microscopy. *Science* **2008**, *322*, 1857–1861.
22. Kukura, P.; McCamant, D. W.; Yoon, S.; Wandschneider, D. B.; Mathies, R. A. Structural Observation of the Primary Isomerization in Vision with Femtosecond-Stimulated Raman. *Science* **2005**, *310*, 1006–1009.
23. Puppels, G. J.; Demul, F. F. M.; Otto, C.; Greve, J.; Robertnico, M.; Arndt-Jovin, D. J.; Jovin, T. M. Studying Single Living Cells and Chromosomes by Confocal Raman Microspectroscopy. *Nature* **1990**, *347*, 301–303.
24. van Manen, H. J.; Kraan, Y. M.; Roos, D.; Otto, C. Single-Cell Raman and Fluorescence Microscopy Reveal the Association of Lipid Bodies with Phagosomes in Leukocytes. *Proc. Natl. Acad. Sci. U.S.A.* **2005**, *102*, 10159–10164.
25. Wu, H. W.; Volponi, J. V.; Oliver, A. E.; Parikh, A. N.; Simmons, B. A.; Singh, S. *In Vivo* Lipidomics Using Single-Cell Raman Spectroscopy. *Proc. Natl. Acad. Sci. U.S.A.* **2011**, *108*, 3809–3814.
26. Kang, B.; Austin, L. A.; El-Sayed, M. A. Real-Time Molecular Imaging throughout the Entire Cell Cycle by Targeted Plasmonic-Enhanced Rayleigh/Raman Spectroscopy. *Nano Lett.* **2012**, *12*, 5369–5375.
27. Austin, L. A.; Kang, B.; El-Sayed, M. A. A New Nanotechnology Technique for Determining Drug Efficacy Using Targeted Plasmonically Enhanced Single Cell Imaging Spectroscopy. *J. Am. Chem. Soc.* **2013**, *135*, 4688–4691.
28. Kimling, J.; Maier, M.; Okenve, B.; Kotaidis, V.; Ballot, H.; Plech, A. Turkevich Method for Gold Nanoparticle Synthesis Revisited. *J. Phys. Chem. B* **2006**, *110*, 15700–15707.
29. Wuelfing, W. P.; Gross, S. M.; Miles, D. T.; Murray, R. W. Nanometer Gold Clusters Protected by Surface-Bound Monolayers of Thiolated Poly(ethylene glycol) Polymer Electrolyte. *J. Am. Chem. Soc.* **1998**, *120*, 12696–12697.
30. Busk, M.; Pytela, R.; Sheppard, D. Characterization of the Integrin alpha-V beta 6 as a Fibronectin-Binding Protein. *J. Biol. Chem.* **1992**, *267*, 5790–5796.
31. Dehari, H.; Ito, Y.; Nakamura, T.; Kobune, M.; Sasaki, K.; Yonekura, N.; Kohama, G.; Hamada, H. Enhanced Antitumor Effect of RGD Fiber-Modified Adenovirus for Gene Therapy of Oral Cancer. *Cancer Gene Ther.* **2003**, *10*, 75–85.
32. Takayama, S.; Hatori, M.; Kurihara, Y.; Kinugasa, Y.; Shirota, T.; Shintani, S. Inhibition of Tgf-beta 1 Suppresses Motility and Invasiveness of Oral Squamous Cell Carcinoma Cell Lines via Modulation of Integrins and Down-Regulation of Matrix-Metalloproteinases. *Oncol. Rep.* **2009**, *21*, 205–210.
33. Xue, H.; Atakilit, A.; Zhu, W. M.; Sheppard, D.; Ramos, D. M.; Pytela, R. Role of alpha(v)beta 6 Integrin in Growth and Migration of Oral Squamous Cell Carcinoma. *Mol. Biol. Cell* **2000**, *11*, 262A.
34. Xue, H.; Atakilit, A.; Zhu, W. M.; Li, X. W.; Ramos, D. M.; Pytela, R. Role of the alpha V beta 6 Integrin in Human Oral Squamous Cell Carcinoma Growth *in Vivo* and *in Vitro*. *Biochem. Biophys. Res. Commun.* **2001**, *288*, 610–618.
35. Dingwall, C.; Laskey, R. A. Nuclear Targeting Sequences—A Consensus. *Trends Biochem. Sci.* **1991**, *16*, 478–481.

36. Robbins, J.; Dilworth, S. M.; Laskey, R. A.; Dingwall, C. 2 Interdependent Basic Domains in Nucleoplasmin Nuclear Targeting Sequence—Identification of a Class of Bipartite Nuclear Targeting Sequence. *Cell* **1991**, *64*, 615–623.
37. Wyllie, A. H. Glucocorticoid-Induced Thymocyte Apoptosis Is Associated with Endogenous Endonuclease Activation. *Nature* **1980**, *284*, 555–556.
38. Marshall, T. Sodium Dodecyl-Sulfate Polyacrylamide-Gel Electrophoresis of Serum after Protein Denaturation in the Presence or Absence of 2-Mercaptoethanol. *Clin. Chem.* **1984**, *30*, 475–479.
39. Woll, M. G.; Hadley, E. B.; Mecozi, S.; Gellman, S. H. Stabilizing and Destabilizing Effects of Phenylalanine → F-5-Phenylalanine Mutations on the Folding of a Small Protein. *J. Am. Chem. Soc.* **2006**, *128*, 15932–15933.
40. Juminaga, D.; Garduno-Juarez, R.; McDonald, M. A.; Scheraga, H. A. Protein Folding Studies of Tyrosine-to-Phenylalanine Substituted Mutants of Ribonuclease A. *Biophys. J.* **1996**, *70*, SU203.
41. Zheng, R.; Zheng, X. J.; Dong, J.; Carey, P. R. Proteins Can Convert to beta-Sheet in Single Crystals. *Protein Sci.* **2004**, *13*, 1288–1294.
42. Thomas, G. J. Raman Spectroscopy of Protein and Nucleic Acid Assemblies. *Annu. Rev. Biophys. Biomol. Struct.* **1999**, *28*, 1–27.
43. Notinger, I.; Hench, L. L. Raman Microspectroscopy: A Noninvasive Tool for Studies of Individual Living Cells *in Vitro*. *Expert Rev. Med. Devices* **2006**, *3*, 215–234.
44. Arai, K. I.; Nakamura, S.; Arai, T.; Kawakita, M.; Kaziro, Y. Limited Hydrolysis of Polypeptide-Chain Elongation Factor Tu by Trypsin Isolation and Characterization of Polypeptide Fragments. *J. Biochem.* **1976**, *79*, 69–83.
45. Hercegova, A.; Sevcovicova, A.; Galova, E. UV Light-Induced DNA Damage Detection in the Unicellular Green Alga *Chlamydomonas reinhardtii*. *Biologia* **2008**, *63*, 958–961.
46. Ruiz-Chica, A. J.; Soriano, A.; Tunon, I.; Sanchez-Jimenez, F. M.; Silla, E.; Ramirez, F. J. FT-Raman and QM/MM Study of the Interaction between Histamine and DNA. *Chem. Phys.* **2006**, *324*, 579–590.
47. Panikanvalappil, S. R.; Mackey, M. A.; El-Sayed, M. A. Probing the Unique Dehydration-Induced Structural Modifications in Cancer Cell DNA Using Surface Enhanced Raman Spectroscopy. *J. Am. Chem. Soc.* **2013**, *135*, 4815–4821.
48. Cerella, C.; Coppola, S.; Maresca, V.; De Nicola, M.; Radogna, F.; Ghibelli, L. Multiple Mechanisms for Hydrogen Peroxide-Induced Apoptosis. In *Natural Compounds and Their Role in Apoptotic Cell Signaling Pathways*; Diederich, M., Ed.; Wiley: New York, 2009; Vol. 1171, pp 559–563.
49. Singh, M.; Sharma, H.; Singh, N. Hydrogen Peroxide Induces Apoptosis in HeLa Cells through Mitochondrial Pathway. *Mitochondrion* **2007**, *7*, 367–373.
50. Austin, L. A.; Kang, B.; Yen, C. W.; El-Sayed, M. A. Plasmonic Imaging of Human Oral Cancer Cell Communities during Programmed Cell Death by Nuclear-Targeting Silver Nanoparticles. *J. Am. Chem. Soc.* **2011**, *133*, 17594–17597.
51. Modesti, M.; Kanaar, R. DNA Repair: Spot(light)s on Chromatin. *Curr. Biol.* **2001**, *11*, R229–R232.
52. Burma, S.; Chen, B. P.; Murphy, M.; Kurimasa, A.; Chen, D. J. ATM Phosphorylates Histone H2ax in Response to DNA Double-Strand Breaks. *J. Biol. Chem.* **2001**, *276*, 42462–42467.
53. Kang, B.; Mackey, M. A.; El-Sayed, M. A. Nuclear Targeting of Gold Nanoparticles in Cancer Cells Induces DNA Damage, Causing Cytokinesis Arrest and Apoptosis. *J. Am. Chem. Soc.* **2010**, *132*, 1517–1519.